

## Comparison of three filters in asteroid-based autonomous navigation<sup>\*</sup>

Wen Cui and Kai-Jian Zhu

State Key Laboratory of Astronautic Dynamics, Xi'an 710043, China; [cuiwen04@gmail.com](mailto:cuiwen04@gmail.com)  
Xi'an Satellite Control Center, Xi'an 710043, China

Received 2013 July 7; accepted 2013 October 7

**Abstract** At present, optical autonomous navigation has become a key technology in deep space exploration programs. Recent studies focus on the problem of orbit determination using autonomous navigation, and the choice of filter is one of the main issues. To prepare for a possible exploration mission to Mars, the primary emphasis of this paper is to evaluate the capability of three filters, the extended Kalman filter (EKF), unscented Kalman filter (UKF) and weighted least-squares (WLS) algorithm, which have different initial states during the cruise phase. One initial state is assumed to have high accuracy with the support of ground tracking when autonomous navigation is operating; for the other state, errors are set to be large without this support. In addition, the method of selecting asteroids that can be used for navigation from known lists of asteroids to form a sequence is also presented in this study. The simulation results show that WLS and UKF should be the first choice for optical autonomous navigation during the cruise phase to Mars.

**Key words:** celestial mechanics — asteroids — equation of state — methods: data analysis — techniques: image processing

### 1 INTRODUCTION

Mars is becoming the focus of most countries interested in space exploration, such as China, Russia and the USA. During the cruise phase to Mars, demonstrating the ability of optical autonomous navigation will be a very meaningful technology. In space missions, autonomous navigation is necessary for the cruise phase when the Sun is between the Earth and the spacecraft. This phenomenon cannot be avoided during missions to Jupiter, Saturn and so on. Although this situation does not necessarily exist in the cruise phase to Mars, it represents a good opportunity to demonstrate the ability of optical autonomous navigation during the cruise phase because the result from orbit determination (OD) with autonomous navigation can be compared with the standard OD result from ground tracking.

With the improvement of onboard imaging and computing technologies, optical autonomous navigation has been an attractive focus of research in interplanetary missions because of its unique advantages compared with ground navigation. The first successful attempt to implement fully automated navigation was the Deep Space 1 mission in 1999 (Bhaskaran et al. 2000). The optical autonomous navigation of this mission was activated during the cruise phase by using images of asteroids to determine the spacecraft's position and velocity (Bhaskaran et al. 2000, 1998a). Subsequently,

---

<sup>\*</sup> Supported by the National Natural Science Foundation of China.

the STARDUST mission used images of comet Wild 2 during the flyby to update information on the target relative state in January, 2004 (Bhaskaran et al. 1998b). During this flyby, the line of sight (LOS) of the comet was incorporated into a Kalman filter to automatically improve the state information. Another successful application of optical autonomous navigation was in the Deep Impact mission in July, 2005. In this mission, Deep Impact used the optical autonomous navigation system to guide the impactor spacecraft to intercept the nucleus of comet Tempel 1 at a location that was illuminated and viewable from the flyby spacecraft (Mastrodemos et al. 2005). It can be expected that optical autonomous navigation will be more commonly used in future planetary explorations.

Besides these cases, almost all previous research works about autonomous navigation have been based on simulations. Recent studies mainly focused on the details of OD problems. A different type of source for optical measurement with OD is analyzed in Tuckness & Young (1995); Zanetti (2009). Stastny and Geller considered the issue of optical autonomous navigation during an approach to Jupiter (Stastny & Geller 2008). Based on a linear covariance analysis, they evaluated the performance of using the optical angles of Jupiter's moons to determine the spacecraft's orbit. The accuracy of optical navigation in three cases by using an unscented Kalman filter (UKF) was presented in Paluszek et al. (2010). The performance of optical autonomous navigation was assessed by applying an extended Kalman filter (EKF) (Christian & Lightsey 2010). However, how to select objects used for navigation during the cruise phase to the planet has rarely been mentioned. This is also a key element involved in optical autonomous navigation. In addition to that, only a single filter such as an EKF, a UKF or a weighted least-squares (WLS) algorithm was used for OD in these papers. An optimal choice of filters would be made if we evaluate the capability of different filters in the mission, especially considering that most studies of optical autonomous navigation have been based on approaching a planet.

To prepare for a future Mars program, the primary emphasis of this paper is to evaluate the performance of the three filters with two different initial states during the cruise phase. One initial state is assumed to have a high accuracy with the support of ground tracking when autonomous navigation is operating; in the other case, state errors are set to large without support. The method of selecting asteroids used for navigation associated with known lists of asteroids to form a sequence is also presented in this study. Data of simulated observations are generated, and we will call these values observation data hereafter. The research shows that a system that uses optical autonomous navigation can successfully navigate during the cruise phase of a Mars mission.

In the following sections, Section 2 gives the nominal transfer orbit of the spacecraft from Earth to Mars. It is the standard orbit to evaluate the precision of OD. Section 3 describes the theory of optical autonomous navigation by using asteroid sighting. Section 4 gives the key elements of optical autonomous navigation. It includes the selection of the asteroids, dynamical model during the cruise phase, observation model and three filtering algorithms. Section 5 gives the results of asteroid selections and analyses the results of three filters with two different initial states. After simulation and analysis, Section 6 gives the conclusions and discussion.

## 2 NOMINAL ORBIT

During the cruise phase of a Mars mission, navigation of the spacecraft will rely on ground tracking stations in the first half of the cruise phase, but navigation during the rest of the phase would be automated by using an onboard camera to take images of asteroids that can be used for triangulation.

Figure 1 illustrates a nominal transfer orbit of the probe from Earth to Mars. In heliocentric coordinates, the blue solid line is the trajectory of the Earth and the black one is that of Mars. Sandwiched between the orbits of Earth and Mars is the spacecraft's trajectory where the red solid line denotes the section where ground tracking is used for navigation of the spacecraft and the green line is the section where optical autonomous navigation is used.

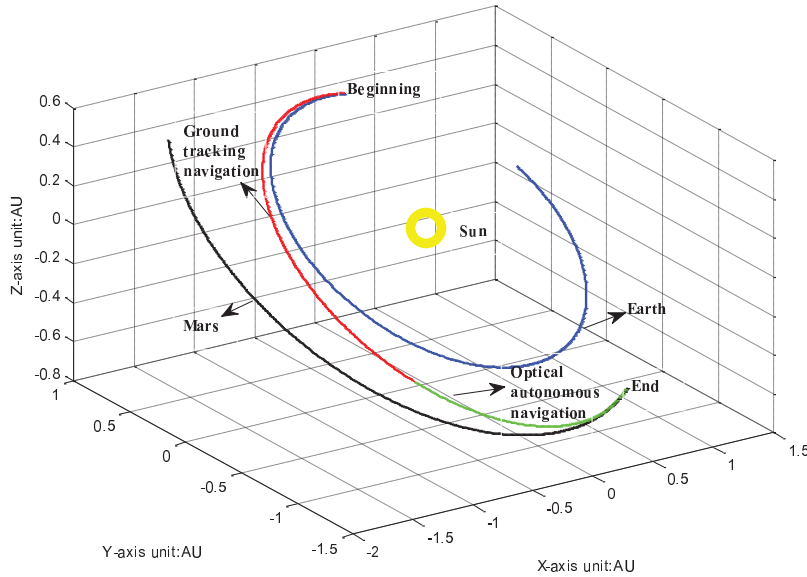


Fig. 1 Trajectory of a spacecraft during the cruise phase to Mars.

Table 1 Orbital Parameters of the Spacecraft

Data Time (TDT)	Position (km)		Velocity (km s <sup>-1</sup> )	
2013-12-11, 17:48:38.168	X-axis	25029930.489	X-axis	-32.434997
	Y-axis	132440957.316	Y-axis	3.781542
	Z-axis	58352343.189	Z-axis	3.418193
2014-05-31, 12:00:00.000	X-axis	-141518043.825	X-axis	14.492278
	Y-axis	-135040735.532	Y-axis	-17.134890
	Z-axis	-53546771.986	Z-axis	-8.471500

Table 1 lists orbital parameters that describe the state of the spacecraft at two important epochs. One state is the beginning of the transfer orbit and the other state is the beginning of the optical autonomous navigation during the cruise phase.

### 3 THEORY OF OPTICAL AUTONOMOUS NAVIGATION

During the cruise phase, the main bodies that can be used for navigation are asteroids. In principle, the theory of optical autonomous navigation by using asteroid sightings is simple. A single sighting of an asteroid places the spacecraft along the LOS to that asteroid. Observing another asteroid at the same time will obtain a second straight line. These two straight lines will determine the heliocentric position of the spacecraft due to the ephemerides of these asteroids, and the inertial pointing directions of the camera are both known at the times the photos are taken.

Figure 2 shows the geometry of optical navigation by using two different asteroids.  $n1$  and  $n2$  are LOSs for two different asteroids respectively.

In practice, however, the field of view (FOV) of the onboard camera used during the cruise phase is extremely narrow; for example, it was  $0.76^\circ$  for the Deep Space 1 mission (Bhaskaran et al. 2000).

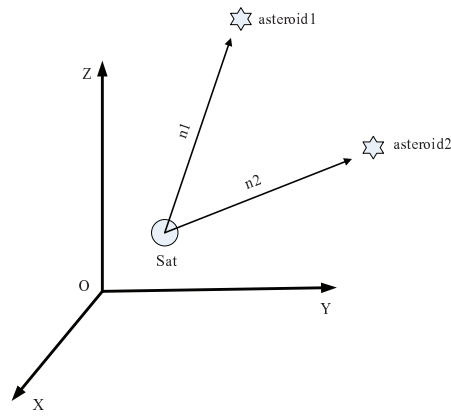


Fig. 2 Schematic diagram of optical navigation by asteroids.

Only one image of an asteroid can be taken at a time. In addition, two sightings are not enough to navigate in a real task because of the error in the asteroid ephemerides, the accuracy in pointing the camera, the resolution of the image, and so on. Instead, a series of LOSs are taken by the onboard camera from one asteroid to another. These images are taken at regular intervals during the cruise phase, with 10 different asteroids sighted per interval in this paper.

## 4 ELEMENTS OF OPTICAL AUTONOMOUS NAVIGATION

### 4.1 Selection of the Asteroids

During the cruise phase, a key technology associated with optical autonomous navigation is the ability to select usable asteroids. The optical measurement provides the sole piece of data that can be used for OD; thus, the accuracy of optical navigation largely depends on the selection of asteroids used for navigation. Typical characteristics of the onboard camera define some selection criteria, including the visible magnitude of the asteroids, the distance between the spacecraft and the asteroids, the velocity of the asteroids relative to the spacecraft, and the phase angle given by the asteroid-spacecraft-Sun (Chausson & Delavault 2003; Delavault et al. 2004). An asteroid will be most identifiable when it is close to the camera. If the asteroid moves too fast with respect to the spacecraft, it will induce a spread on the picture that will reduce accuracy in the astrometric measurement. A proper phase angle can prevent sunlight from contaminating the focal plane of the CCD in the camera. In addition, the geometry of different asteroids with respect to the spacecraft, given by the angle asteroid1-spacecraft-asteroid2, is another important factor that should be considered during the process of selection.

All the selection criteria mentioned above are easy to understand except the visible magnitude of the asteroids. The larger the visible magnitude of an asteroid is, which corresponds to a fainter object, the more difficult it is for the camera to capture it. The magnitude can be calculated by the Bowell model (Romanishin & Tegler 2005):

$$\begin{aligned} V &= H_0 + 5 \ln(r_0 d_0) - 2.5 \ln[(1 - G) \Phi_1(\alpha) + G \Phi_2(\alpha)], \\ \Phi_i(\alpha) &= \exp[-A_i \tan^{B_i}(\frac{\alpha}{2})], \end{aligned} \quad (1)$$

where  $H_0$  and  $G$  are the absolute magnitude and albedo parameter respectively, which can be obtained from a database of asteroids;  $r_0$  is the heliocentric distance of the spacecraft in units of AU;  $d_0$  is the distance between the spacecraft and the observed asteroid in units of AU;  $\alpha$  is the phase angle

**Table 2** Selection Criteria for Asteroids Used in Navigation

Selection Criteria	Threshold Value
Visible magnitude	< 12.9
Phase angle	> 130.0°
Relative distance	< 2.0 AU
Relative velocity	< 11.8 km s <sup>-1</sup>
Geometric angle	> 5.0°

defined by the Sun-asteroid-spacecraft; and  $i = 1, 2$ ,  $A_1 = 3.33$ ,  $B_1 = 0.63$ ;  $A_2 = 1.87$ ,  $B_2 = 1.22$ .

By referencing parameters on the optical system of the Deep Space 1 mission (Bhaskaran et al. 2000, 1998a), Table 2 shows the criteria and associated thresholds for the selection of asteroids that can be used during the cruise phase.

Based on the above selection criteria, asteroids that can be used for navigation can be selected by following these three steps:

- (1) A preliminary screening from the whole asteroid database should be made by restricting the absolute magnitude and orbital semi-major axis of the asteroids. Only 1% of asteroids, the quantity which is on the order of thousands, can remain. We call this sequence A.
- (2) According to the nominal orbit during the cruise phase and the ephemeris of asteroids, the selection criteria presented in Table 2, except for the last one, can be performed for every asteroid in sequence A. Sequence B is obtained when this process is accomplished. Sequence B only has dozens of asteroids in this study.
- (3) If the number of asteroids in sequence B is more than the required number, which is ten in this paper, the angles (asteroid1-spacecraft-asteroid2) defined for every two different asteroids in sequence B should be calculated. Then, a statistical result on the geometric angle which is below the threshold value in Table 2 for each asteroid will be found. The asteroid which appears repeatedly in the statistical result will be omitted until the total number of asteroids in sequence B is equal to ten. If the total number in the original sequence B is less than ten, the selection process ends, but this situation rarely occurs.

A group of asteroids used for navigation should be varied with the epoch; and furthermore, the spacecraft and the asteroids are constantly in motion. According to the nominal trajectory of the spacecraft, the cruise phase to Mars will be divided into several periods and the length of each period is 10 d. The sequence of asteroids used for navigation is independent in each period.

#### 4.2 Dynamical Model During the Cruise Phase

The main force acting on the spacecraft during the cruise phase to Mars is gravity from the Sun; in addition to that, third body perturbations from the gravity of other major planets should also be considered. Therefore, the dynamical model describing the trajectory of the spacecraft during the cruise phase to Mars in the J2000 heliocentric ecliptic coordinate system can be written as follows:

$$\begin{aligned} \dot{\mathbf{r}} &= \mathbf{v}, \\ \ddot{\mathbf{r}} &= -\frac{\mu_s}{r^3} \mathbf{r} + \sum_{k=1}^8 \mu_k \left( \frac{\mathbf{r}_{rk}}{r_{rk}^3} - \frac{\mathbf{r}_{pk}}{r_{pk}^3} \right) + \mathbf{a}, \end{aligned} \quad (2)$$

where  $\mathbf{r}$  and  $\mathbf{v}$  are, respectively, the position and velocity vectors of the spacecraft in the J2000 heliocentric coordinate system,  $r = \|\mathbf{r}\|$ ;  $\mu_s = GM_s$ , where  $G$  is the gravitational constant and  $M_s$  is the mass of the Sun, and  $\mu_k = GM_k$ , where  $M_k$  is the mass of major planets;  $\mathbf{r}_{pk}$  is the position vectors of the  $k$ -th planet in the J2000 heliocentric coordinate system,  $r_{pk} = \|\mathbf{r}_{pk}\|$ ;  $\mathbf{r}_{rk}$  is

the position vector of the  $k$ -th planet relative to the spacecraft, i.e.,  $\mathbf{r}_{rk} = \mathbf{r}_{pk} - \mathbf{r}$ ,  $r_{rk} = \|\mathbf{r}_{rk}\|$ ;  $\mathbf{a}$  is the miscellaneous force acting on the spacecraft, including solar radiation pressure and similar effects.

### 4.3 Model of Observation Data

When an image of an asteroid is taken that has stars in the background, the pixel and line (the  $x$  and  $y$  coordinate in the CCD plane) which contain the LOS to the asteroid can be calculated by combining them with a pre-stored star chart. Actually, the pixel and line are the sole observation data used for autonomous navigation. The relationship between the position of the spacecraft and the observed data will be given in the following description (Bhaskaran et al. 1998b; Jacobson 1998).

In J2000 heliocentric ecliptic coordinates,  $(x \ y \ z)^T$  is the position vector of the spacecraft at the time the photo is acquired, and the associated position vector of the asteroid is  $(x_i \ y_i \ z_i)^T$  which can be obtained from the asteroid database. Consequently, the LOS vector of the asteroid with respect to the spacecraft in inertial coordinates can be written as

$$\mathbf{n} = (n_x \ n_y \ n_z)^T = \frac{1}{\sqrt{(x_i - x)^2 + (y_i - y)^2 + (z_i - z)^2}} \begin{bmatrix} x_i - x \\ y_i - y \\ z_i - z \end{bmatrix}. \quad (3)$$

$A_{bo}$  is the rotation matrix of inertial coordinates with respect to body-fixed coordinates of the camera, which is provided by the attitude determination and control system of the spacecraft. Thus, the LOS vector  $\mathbf{n} = (n_x \ n_y \ n_z)^T$  mentioned above in body-fixed coordinates of the camera is given by

$$\mathbf{n}_b = (n_{bx} \ n_{by} \ n_{bz})^T = A_{bo}\mathbf{n}. \quad (4)$$

Then, vector  $\mathbf{n}_b$  needs to be projected into the focal plane of the onboard camera, viz.

$$\begin{bmatrix} X \\ Y \end{bmatrix} = \frac{f}{n_{bz}} \begin{bmatrix} n_{bx} \\ n_{by} \end{bmatrix}, \quad (5)$$

where  $f$  is the focal length of the onboard camera in units of mm;  $n_{bx}$ ,  $n_{by}$ ,  $n_{bz}$  are the components of the vector  $\mathbf{n}_b$ ;  $X$ ,  $Y$  is the projection of the LOS vector in the focal plane.

In order to simplify the model of observation data, the electromagnetic distortion and optical aberration of the onboard camera do not need to be included in  $X$ ,  $Y$ .

Thus, the camera pixel and line which can be translated from  $X$ ,  $Y$  is

$$\begin{bmatrix} p \\ l \end{bmatrix} = K \begin{bmatrix} X \\ Y \end{bmatrix} + \begin{bmatrix} p_0 \\ l_0 \end{bmatrix} = \frac{f}{n_{bz}} \begin{bmatrix} K_x & 0 \\ 0 & K_y \end{bmatrix} \begin{bmatrix} n_{bx} \\ n_{by} \end{bmatrix} + \begin{bmatrix} p_0 \\ l_0 \end{bmatrix}, \quad (6)$$

where  $p$ ,  $l$  are the camera pixel and line associated with different asteroids respectively;

$$K = \begin{bmatrix} K_x & 0 \\ 0 & K_y \end{bmatrix}$$

is a transformation matrix from mm to pixels in the camera in the unit of mm/pixel;  $p_0$ ,  $l_0$  are the center pixel and line of the CCD plane respectively.

Assuming  $p_0 = 0$ ,  $l_0 = 0$ , and accounting for error in the measurement process, the equation describing observation data can be derived as

$$\mathbf{Z} = \begin{bmatrix} p \\ l \end{bmatrix} + \nu = \frac{f}{n_{bz}} \begin{bmatrix} K_x & 0 \\ 0 & K_y \end{bmatrix} \begin{bmatrix} n_{bx} \\ n_{by} \end{bmatrix} + \nu, \quad (7)$$

where  $\nu$  is the measurement noise, which is always treated as Gaussian white noise.

#### 4.4 Filtering Algorithms

Once the observation data are generated, the solution of the position and velocity parameters which are corrections to the initial state for the spacecraft can be obtained using filtering technology. Two kinds of filtering methods are commonly used in space navigation. One is batch filtering, whose typical representative is the WLS algorithm; the other is recursive processing algorithms including EKF, UKF and so on. The WLS algorithm has been successfully applied in optical autonomous navigation of the Deep Space 1 and Deep Impact missions, and the EKF has also been successfully applied in the STARDUST mission (Bhaskaran et al. 1998a,b; Mastrodemos et al. 2005). Each filter algorithm has its own advantages (Daum 2005). Here, the capability of these three filters (WLS, EKF and UKF) used in optical autonomous navigation will be compared during the cruise phase to Mars.

##### 4.4.1 Weighted least squares method (Long et al. 1989)

The definition of state parameters that need to be updated is

$$\mathbf{q}(t) = [x(t) \ y(t) \ z(t) \ \dot{x}(t) \ \dot{y}(t) \ \dot{z}(t)]^T. \quad (8)$$

In real task, the true value of  $\mathbf{q}(t)$  is unknown. Thus, we can just calculate the optimal estimated value by replacing  $\mathbf{q}(t)$ . The initial value is known. It can be used as the approximate value of  $\mathbf{q}(t)$ , then we can obtain

$$\bar{\mathbf{q}}(t) = \mathbf{q}^*(t) + \Delta\mathbf{q}(t), \quad (9)$$

by incorporating the observation data, where  $\bar{\mathbf{q}}(t)$  is the optimal estimated value of the true value,  $\mathbf{q}^*(t)$  is the initial value, and  $\Delta\mathbf{q}(t)$  is the vector of estimated corrections by the observation data.

Next we will calculate  $\Delta\mathbf{q}(t)$  by WLS. The model in Equation (7) is nonlinear; thus, the partial derivatives of the estimated state are needed when using WLS. At the time of the observation, the partial matrix of state  $\mathbf{q}(t)$  can be written as

$$H_i = \frac{\partial Z_i}{\partial \mathbf{q}} = \begin{bmatrix} \frac{\partial p}{\partial x} & \frac{\partial p}{\partial y} & \frac{\partial p}{\partial z} & 0 & 0 & 0 \\ \frac{\partial l}{\partial x} & \frac{\partial l}{\partial y} & \frac{\partial l}{\partial z} & 0 & 0 & 0 \end{bmatrix}, \quad (i = 1, 2, \dots, n), \quad (10)$$

where  $n$  is the number of asteroids used for navigation.

Different observation data can be used in different epochs. Therefore, a state transition matrix  $\Phi(t_0, t)$  is needed to map the partial matrix  $H$  back to the epoch associated with the estimated state.

$$\tilde{H} = \begin{bmatrix} H_1 \Phi(t_0, t_1) \\ H_2 \Phi(t_0, t_2) \\ \dots \\ H_n \Phi(t_0, t_n) \end{bmatrix}, \quad (11)$$

where  $\tilde{H}$  is the matrix of observation data at the epoch associated with the estimated state.

The state transition matrix  $\Phi(t_0, t)$  can be found by

$$\begin{cases} \dot{\Phi}(t_0, t) = \frac{\partial \dot{\mathbf{q}}(t)}{\partial \mathbf{q}(t)} \Phi(t_0, t) \\ \Phi(t_0, t_0) = \mathbf{I}_{6 \times 6} \end{cases}, \quad (12)$$

where  $\mathbf{I}_{6 \times 6}$  is a  $6 \times 6$  unit matrix.

Given the a priori covariance matrix  $P_0$  of state parameters and the weighted matrix  $W$  from observations, the filter equations in batch form can be written as

$$\begin{aligned}\Delta \mathbf{q}_k(t) &= \left[ P_k^{-1} + \tilde{H}^T W \tilde{H} \right]^{-1} \tilde{H}^T W \left( Z - \tilde{Z}_k \right), \\ \mathbf{q}_{k+1}(t) &= \mathbf{q}_k(t) + \Delta \mathbf{q}_k(t), \\ P_{k+1} &= \left[ P_k^{-1} + \tilde{H}^T W \tilde{H} \right]^{-1}, \\ k &= 1, 2, 3, \dots,\end{aligned}\quad (13)$$

where  $P_k$  is the covariance matrix;  $Z$  is the observed value; and  $\tilde{Z}_k$  is the value predicted by the model.

#### 4.4.2 Extended Kalman filter (Long et al. 1989; Pittelkau 2003)

Equations (2) and (7) are both nonlinear. The EKF simplifies these two sets of equations with a first-order Taylor series evaluated at the estimated state  $\mathbf{q}(t)$  mentioned above. Hence, Equations (2) and (7) should be linearized at  $\mathbf{q}(t)$ . The Jacobi matrix for Equation (7) can be derived as

$$H_E = \begin{bmatrix} H_1 \\ H_2 \\ \dots \\ H_n \end{bmatrix}, \quad (14)$$

where  $H_i (i = 1..n)$  can be found according to Equation (10).

The Jacobi matrix of dynamical Equation (2) can be written as

$$F = \frac{\partial \dot{\mathbf{q}}(t)}{\partial \mathbf{q}(t)} = \begin{bmatrix} 0_{3 \times 3} & \mathbf{I}_{3 \times 3} \\ U & 0_{3 \times 3} \end{bmatrix}, \quad (15)$$

where

$$U = -\frac{\mu_s}{r^3} \mathbf{I}_{3 \times 3} + \frac{3\mu_s}{r^5} \mathbf{r} \mathbf{r}^T - \sum_{k=1}^8 \mu_k \left( \frac{1}{r_{rk}^3} \mathbf{I}_{3 \times 3} + \frac{3}{r_{rk}^5} \mathbf{r}_{rk} \mathbf{r}_{rk}^T \right).$$

Now, the mathematical processes of the EKF can be detailed in the following steps.

(1) The propagations of the estimated state and the covariance matrix are defined as

$$\begin{aligned}\mathbf{q}_{k|k-1}(t) &= f_0(\mathbf{q}_{k-1}(t)), \\ P_{k|k-1} &= \Phi_{k,k-1} P_{k-1} \Phi_{k,k-1}^T + Q_k,\end{aligned}\quad (16)$$

where  $f_0$  is integrated from the dynamical Equation (2);  $\Phi_{k,k-1}$  is the state transition matrix from the  $(k-1)$ -th step to the  $k$ -th step; according to Equation (15), the approximate calculation is  $\Phi_{k,k-1} \approx \mathbf{I}_{6 \times 6} + F|_{\mathbf{q}_{k|k-1}} \cdot (t_k - t_{k+1})$ ;  $Q_k$  is the noise covariance matrix of the estimated state.

(2) Calculate the Kalman gain matrix  $K_k$ ,

$$K_k = P_{k|k-1} H_{Ek}^T \left[ H_{Ek} P_{k|k-1} H_{Ek}^T + R_k \right]^{-1}, \quad (17)$$

where  $R_k$  is the covariance matrix of measurement noise;  $H_{Ek}$  is the  $k$ -th matrix of observation data which can be obtained from Equation (14).

(3) Update the estimated state and covariance matrices

$$\begin{cases} \mathbf{q}_k(t) = \mathbf{q}_{k|k-1}(t) + K_k \left[ Z_k - \tilde{Z}_k(\mathbf{q}_{k|k-1}(t)) \right], \\ P_k = (\mathbf{I}_{6 \times 6} - K_k H_{Ek}) P_{k|k-1}, \end{cases} \quad (18)$$

where  $Z_k$  is the observation data;  $\tilde{Z}_k$  is the value calculated by the model.

#### 4.4.3 Unscented Kalman filter

The UKF is a new Kalman filter for a nonlinear system invented by Julier and Uhlmann (Julier & Uhlmann 1997). Unlike the EKF, the Jacobi matrices of the dynamical equations and equations describing observational data are not required, and neither is the state transition matrix. The key point of the UKF is based on an unscented transformation (UT) which uses a set of appropriately chosen weighted points to parameterize the mean and covariance of the probability distributions. A detailed description of UKF theory can be found in the article (Julier & Uhlmann 2004). A brief description of using the UKF will be given here.

Firstly, the UT is introduced as follows.

For a given nonlinear equation  $\mathbf{y} = g(\mathbf{x})$ , the  $n$ -dimensional estimated state  $\mathbf{x}$  with mean  $\bar{\mathbf{x}}$  and covariance  $P_{xx}$  is approximated by  $2n + 1$  weighted points given by

$$\begin{cases} \chi_0 = \bar{\mathbf{x}}, & w_0 = \frac{\kappa}{n+\kappa}, \\ \chi_i = \bar{\mathbf{x}} + \sqrt{n+\kappa} (\sqrt{P_{xx}})_i, & w_i = \frac{\kappa}{2(n+\kappa)}, \\ \chi_{i+n} = \bar{\mathbf{x}} - \sqrt{n+\kappa} (\sqrt{P_{xx}})_i, & w_{i+n} = \frac{\kappa}{2(n+\kappa)}, \\ i = 1 \dots n, \end{cases} \quad (19)$$

where  $\kappa \in R$ , and it usually has  $n + \kappa = 3$  when  $\mathbf{x}$  is assumed to have a Gaussian distribution. In our study, the dimension of the state is 6; thus,  $\kappa = -3$ ;  $(\sqrt{P_{xx}})_i$  is the  $i$ -th column of the matrix square root of  $P_{xx}$ ;  $w_i$  is the weight associated with the  $i$ -th point.

Therefore, the mean of  $\mathbf{y}$  can be calculated by the weighted average of the transformed points,

$$\bar{\mathbf{y}} = \sum_{i=0}^{2n} w_i g(\chi_i) \quad (20)$$

and the covariance of  $\mathbf{y}$  can be obtained by

$$P_{yy} = \sum_{i=0}^{2n} w_i [g(\chi_i) - \bar{\mathbf{y}}] [g(\chi_i) - \bar{\mathbf{y}}]^T. \quad (21)$$

Given the initial estimated state  $\mathbf{q}(t_0)$  and the initial covariance matrix  $P_0$ , the UKF can proceed similarly to the EKF.

- (1) Create a set of weighted points by Equation (19) where  $\bar{\mathbf{x}} = \mathbf{q}(t_0)$  and  $P_{xx} = P_0$  at the beginning.
- (2) Propagate the estimated state and the covariance matrix as

$$\begin{aligned} \chi_{i,k|k-1} &= f(\chi_{i,k-1}), \\ \mathbf{q}_{k|k-1}(t) &= \sum_{i=0}^{2n} w_i \chi_{i,k|k-1}, \\ P_{xx,k|k-1} &= \sum_{i=0}^{2n} w_i [\chi_{i,k|k-1} - \mathbf{q}_{k|k-1}(t)] [\chi_{i,k|k-1} - \mathbf{q}_{k|k-1}(t)]^T + Q_k, \end{aligned} \quad (22)$$

where  $f$  is integrated from the dynamical Equation (2);  $n = 6$  is the dimension of the estimated state.

- (3) The prediction of the observation and its covariance matrix is

$$\begin{aligned} \gamma_{i,k|k-1} &= h(\chi_{i,k|k-1}), \\ \tilde{\mathbf{Z}}_{k|k-1} &= \sum_{i=0}^{2n} w_i \gamma_{i,k|k-1}, \\ P_{zz,k|k-1} &= \sum_{i=0}^{2n} w_i [\gamma_{i,k|k-1} - \tilde{\mathbf{Z}}_{k|k-1}] [\gamma_{i,k|k-1} - \tilde{\mathbf{Z}}_{k|k-1}]^T + R_k, \end{aligned} \quad (23)$$

where  $h$  is the observation described Equation (7);  $R_k$  is the covariance matrix of measurement noise.

(4) Calculate the Kalman gain matrix  $K_k$

$$\begin{aligned} P_{xz,k|k-1} &= \sum_{i=0}^{2n} w_i \left[ \chi_{i,k|k-1} - \mathbf{q}_{k|k-1}(t) \right] \left[ \gamma_{i,k|k-1} - \tilde{Z}_{k|k-1} \right]^T, \\ K_k &= P_{xz,k|k-1} P_{zz,k|k-1}^{-1}. \end{aligned} \quad (24)$$

(5) Update the estimated state and the covariance matrix

$$\begin{aligned} \mathbf{q}_k(t) &= \mathbf{q}_{k|k-1}(t) + K_k \left[ Z_k - \tilde{Z}_{k|k-1} \right], \\ P_{xx,k} &= P_{xx,k|k-1} - K_k P_{zz,k|k-1} K_k^T. \end{aligned} \quad (25)$$

where  $Z_k$  is the observation data.

## 5 SIMULATION AND RESULTS

### 5.1 Initial Conditions

When the model describing observation data and the filter algorithm are chosen, there are a series of initial conditions that need to be applied in order to derive results. These parameters directly affect the accuracy of the derived OD. The accuracy of the OD solution depends on several factors, including the a priori knowledge of error in position and velocity, the error in the asteroid ephemeris, the ability to pinpoint the location of the asteroid in the CCD plane (finding its center), the accuracy of the inertial pointing direction of the camera, the number of the asteroids used for navigation, the frequency of imaging, the miscellaneous force acting on the spacecraft and the choice of filter.

Based on the actual tasks performed during deep space exploration or scientific research, the value of each parameter has a recommended range. The a priori accuracies in the state can be determined to a few kilometers in position and less than  $0.1 \text{ m s}^{-1}$  in velocity (Cao et al. 2010; MacKenzie et al. 2004) with the help of the ground OD results that are sent when the optical autonomous navigation operates. Otherwise, the error is set to be 5000 km in position and  $10 \text{ m s}^{-1}$  in velocity for each axis. An assumption of optical autonomous navigation by asteroids is that the heliocentric positions of the asteroids are known exactly at the time their photo is taken. However, this is not necessarily true. The error in asteroid ephemeris is on the order of tens of kilometers if this asteroid is larger, brighter or has long periods of tracking, but that for the smaller, dimmer ones can be several hundreds of kilometers (Bhaskaran et al. 1998a). For the purpose of keeping the onboard OD algorithm simple, the error in asteroid ephemeris is set to be 100 km for a  $1\sigma$  uncertainty in standard deviation along each axis. The center of the asteroid in the camera frame at the time the photo is taken and the associated pointing of the camera boresight mainly depends on the image processing system. The process of autonomous navigation relies on its ability to accurately find the center. The method used for finding the center can achieve an accuracy of up to 0.1 pixel and the inertial pointing direction of the camera can be determined to within a few  $\mu\text{rad}$  from experimental results (Bhaskaran et al. 2000, 1998a). The image of each asteroid is taken at 5-day intervals during the cruise, with 10 different asteroids sighted per interval in this paper. During the latter half of the cruise phase to Mars, the solar radiation pressure, which is not included in the model, adds a small acceleration of about  $2.2 \times 10^{-7} \text{ m s}^{-2}$  based on a simple spherical model. A summary of the different factors which limit the performance of the OD solutions and their chosen values are listed in Table 3. The parameters of the onboard camera are similar to those of the MICAS camera system, which is coupled to a telescope with a focal length of 677 mm and a standard CCD chip with a 1024 square pixel array. Each pixel has an FOV of about  $13 \mu\text{rad}$  for a total FOV of  $0.76^\circ$ .

**Table 3** Summary of the Factors and Their Values

Different factors	Setting values
A priori state error	5000 km and 10 m s <sup>-1</sup> per axis (alternative 5 km and 0.1 m s <sup>-1</sup> )
Asteroid ephemeris error	100 km
Ability of finding the center	0.1 pixel
Accuracy of pointing direction	3 rad
Number of navigation asteroids	10
Imaging frequency	5 day
Miscellaneous outside acceleration	$2.2 \times 10^{-7}$ m s <sup>-2</sup>
Filtering algorithm	WLS, EKF, UKF

**Table 4** Asteroid Sequence for Optical Navigation

Period code	Period (MJD)	Minor planet number
1	56808.5~56818.5	1, 9, 43, 68, 117, 199, 363, 438, 480, 891
2	56818.5~56828.5	9, 13, 68, 75, 117, 199, 363, 480, 751, 891
3	56828.5~56838.5	9, 13, 75, 108, 190, 198, 480, 751, 891, 1043
4	56838.5~56848.5	9, 13, 65, 108, 190, 198, 363, 480, 891, 1043
5	56848.5~56858.5	9, 13, 15, 22, 108, 190, 198, 363, 480, 891
6	56858.5~56868.5	9, 13, 15, 22, 61, 108, 190, 198, 769, 891
7	56868.5~56878.5	9, 13, 15, 22, 61, 190, 198, 257, 463, 769
8	56878.5~56888.5	13, 15, 22, 61, 146, 190, 198, 463, 510, 1043
9	56888.5~56898.5	13, 15, 22, 29, 61, 146, 198, 463, 510, 1043
10	56898.5~56908.5	13, 15, 22, 29, 61, 146, 257, 463, 510, 1043
11	56908.5~56918.5	13, 15, 22, 61, 146, 164, 354, 463, 510, 1043
12	56918.5~56928.5	13, 15, 22, 29, 61, 106, 146, 164, 463, 510

## 5.2 Results of Asteroid Selections

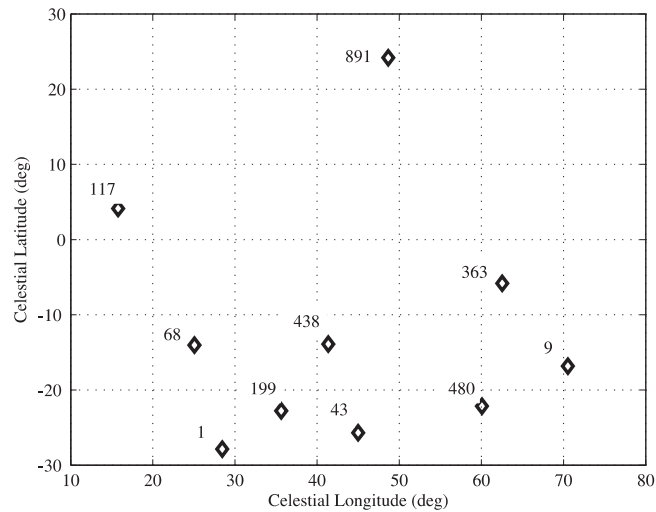
According to the selection criteria listed in Table 2 and the selection methods mentioned in Section 4.1, as applied to the nominal transfer orbit to Mars, the sequence of asteroids used for each period of optical navigation is listed in Table 4. It can be easily noted from Table 4 that there is only a small difference between the two adjacent sequences of asteroids. The small difference is mainly caused by the movement of asteroids during navigation and cannot be ignored.

Figure 3 illustrates the celestial longitude and celestial latitude of asteroids used for navigation in the J2000 spacecraft-body ecliptic coordinate system at the epoch MJD= 56813.5. The diamonds denote the various asteroids and their associated minor planet numbers. The intuitive reason that this group of asteroids would be an excellent choice for navigation is that it has convenient geometry.

After the asteroids are selected, the observation data can be generated as follows. The spacecraft-to-asteroid vector is calculated by using the true spacecraft trajectory and a contaminated asteroid ephemeris which is added at random with the noise having a zero mean and a given standard deviation. Then the vector is transformed into the plane of the camera by applying the model describing the observational data. During the transformation, the error in the pointing direction and measurement error mentioned in Table 3 are added.

## 5.3 Results of OD

At the beginning of the optical autonomous navigation, the initial state error of the spacecraft is assumed to have two cases. One is 5000 km in position and 10 m s<sup>-1</sup> in velocity for each axis. This case indicates that there is no assistance from the ground tracking OD results at the moment. The other case is 5 km in position and 0.1 m s<sup>-1</sup> in velocity along each axis. This situation needs the



**Fig. 3** Distribution of navigation asteroids at the epoch MJD = 56813.5 in the J2000 spacecraft-body ecliptic coordinate system.

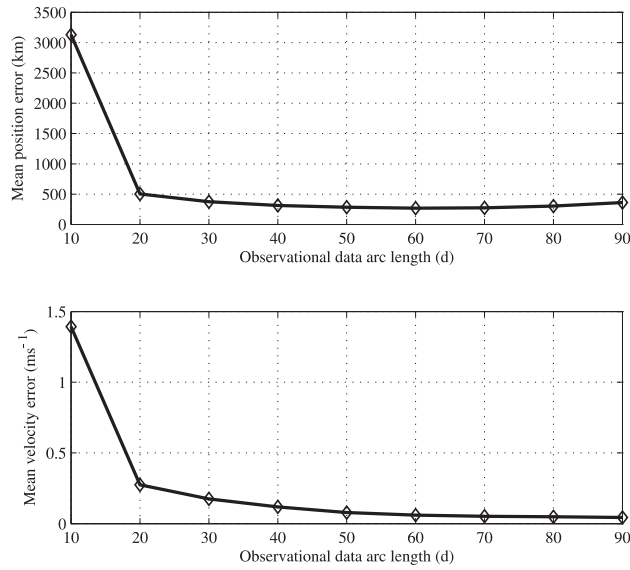
OD results from the ground stations. For both cases, the navigation performance by only using the optical measurement of LOS will be evaluated during the cruise phase to Mars. In addition to that, the capability of three different filtering algorithms which include WLS, EKF and UKF can also be assessed for these two cases. Then the analysis for these two cases is given as follows.

**(1) The initial state error is 5000 km in position and  $10 \text{ m s}^{-1}$  in velocity along each axis.**

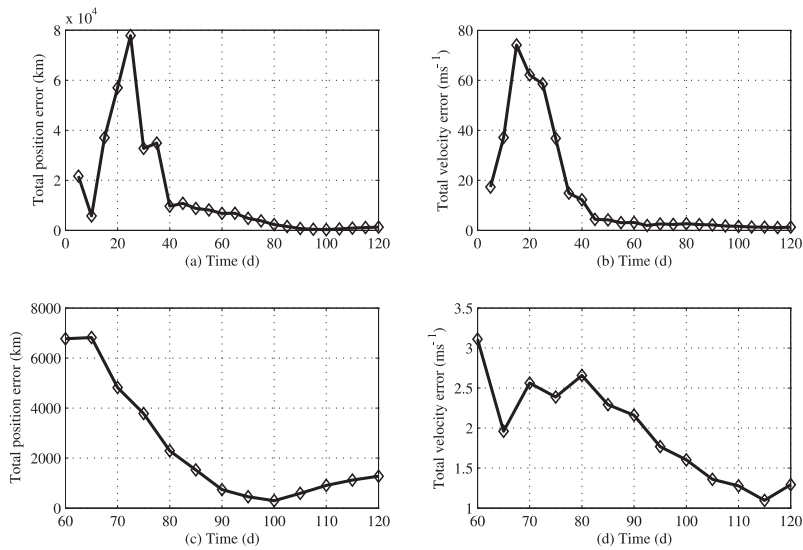
In this situation, the position and velocity errors are compared with the nominal trajectory by using the three different filtering algorithms and are shown in Figures 4, 5 and 6, respectively.

Figure 4 illustrates a result by using the WLS algorithm. In Figure 4, the mean position and velocity errors are plotted as a function of arc length where data are observed. It can be seen that the mean errors for both position and velocity have obviously been reduced when the data spanning 10, 20 and 30 d are used, but then they rapidly level off even if the length of time that the data are taken is at least doubled. This phenomenon is mainly due to the miscellaneous force acting on the spacecraft and other sources of error mentioned in Table 3. These error sources hinder the added data from achieving a better result after 30 d, but a balanced solution can be achieved. A better result cannot be obtained if the state error of the spacecraft has already decreased to a certain level. This level is about  $300 \sim 400 \text{ km}$  in total position and  $0.05 \sim 0.1 \text{ m s}^{-1}$  in total velocity, as seen in Figure 4. For this reason, 30 d can be chosen to be an optimal arc length over which data can be acquired. This strategy can supply enough information to obtain an OD solution with proper accuracy if the filtering algorithm is the WLS in optical autonomous navigation.

Figures 5 and 6 show the total position and velocity errors by using EKF and UKF, respectively. The top two plots of Figure 5 illustrate the state error during the whole autonomous navigation segment which lasts 120 d, and the bottom two plots only show a portion of the result of the top two plots when the EKF begins to converge 60 d later. In the last 30 d, the EKF's result maintains a stable state, for which errors are about  $1000 \text{ km}$  in total position and  $1 \sim 2 \text{ m s}^{-1}$  in total velocity. The layout of Figure 6 for UKF is the same as Figure 5. From Figure 6, it can be found that the filtering result begins to converge 20 d later. The position errors are reduced to about  $200 \sim 400 \text{ km}$  and the velocity errors are about  $0.05 \sim 0.1 \text{ m s}^{-1}$  in the last 60 d. It follows that the UKF is able



**Fig. 4** Errors in position and velocity by using WLS.



**Fig. 5** Position and velocity errors by using EKF. (a) and (b) are the position and velocity errors respectively during the entire segment where autonomous navigation is used; (c) and (d) are the corresponding results of the convergent portion during the autonomous navigation, respectively.

to achieve a better performance at estimation, including the convergence rate and the convergence precision, than the EKF in this case. During the whole filtering process, the fluctuation in amplitude of UKF is also much less than that of EKF. This is due to the unscented transformation (UT) used in UKF. The UT allows the UKF to capture the first and second order terms of the nonlinear system (VanDyke et al. 2004), but the EKF is just based on a simple linear approximation to the nonlinear equations (Daum 2005). Moreover, the dynamical equations and the observation equations are both

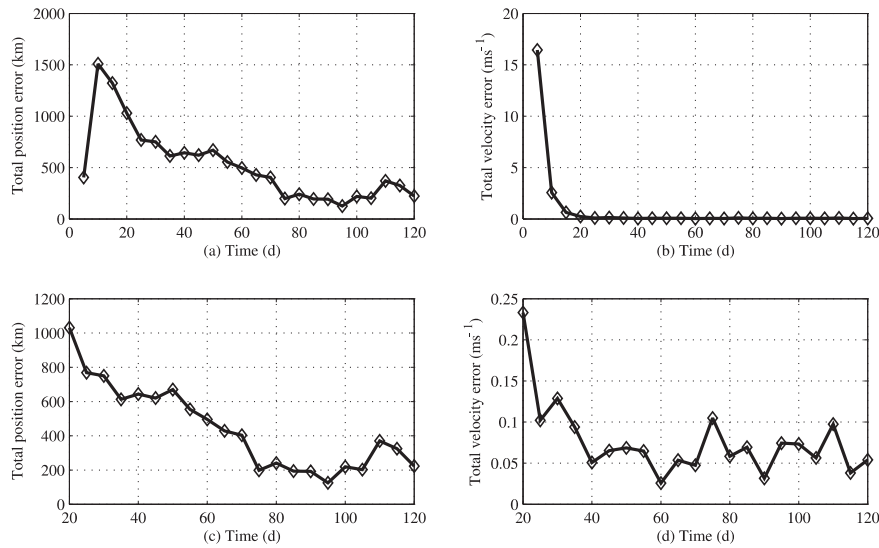


**Fig. 6** Position and velocity errors by using UKF. (a) and (b) are the position and velocity errors respectively during the entire segment where autonomous navigation is used; (c) and (d) are the corresponding results of the convergent portion during the autonomous navigation, respectively.

nonlinear equations, and the initial state errors are too large. Therefore, the result from estimation with UKF is vastly superior to the estimation with EKF in this situation.

According to the above analysis, the performances of the WLS and the UKF are almost the same in this case, although WLS is a batch filtering algorithm and UKF is a recursive processing algorithm. Also, they are both superior to the EKF. Although the WLS relies on a linear approximation during the process like the EKF, the WLS updates the estimated state based on batch data whereas the EKF only uses the last single data to improve the state. Up to now, the WLS has already been successfully used in the Deep Space 1 mission during the cruise phase (Bhaskaran et al. 1998a); maybe the UKF can also undertake this important role.

## (2) The initial state error is 5 km in position and 0.1 m s<sup>-1</sup> in velocity for each axis.

The initial state error used here is much smaller than the above situation due to the OD results incorporating the ground uplink at the beginning of the optical autonomous navigation.

Figures 7 and 8 give the total position and velocity errors by using the EKF and UKF in this case. There is no WLS result here because the WLS always converges to a unique solution only if the initial state error is in an appropriate range. That is to say, the WLS result in this case is the same as the above case, so there is no need for further analysis of WLS.

Figure 7 shows the total position error by using EKF and UKF in different line styles, and Figure 8 is the same layout for total velocity error. From these two plots, both of them obtain a good quality result, and the result from UKF is only slightly better than that from EKF, which is because the initial state already has to achieve a high accuracy; just a small quantity of data can help these two filters overcome the error sources to reach a steady solution. At the beginning, the rapid increase in position and velocity errors during a short time is due to the errors from observed data. However, it quickly achieves a stable state under the action of the filter. For both EKF and UKF, the state error is about 200~400 km in position and 0.05~0.1 m s<sup>-1</sup> in velocity when the filtering result reaches a stable state. This result is almost the same as the case that has a large initial error state for UKF, but for

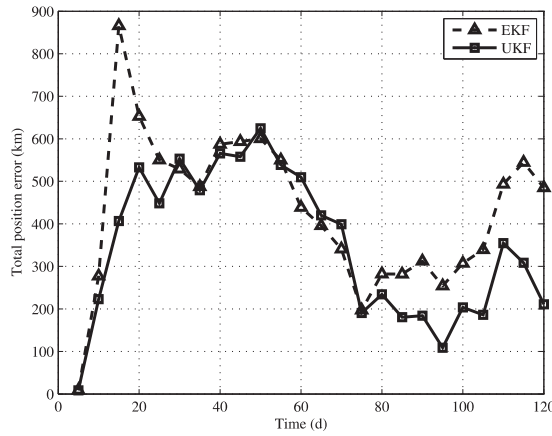


Fig. 7 Position errors by using EKF and UKF.

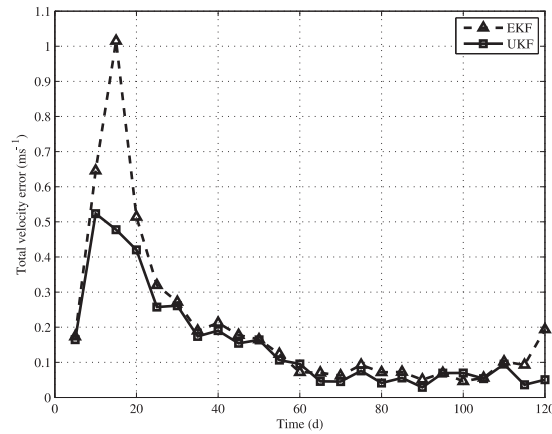


Fig. 8 Velocity errors by using EKF and UKF.

EKF this situation is much better than the above case, which indicates that the EKF has not reached a real steady state until the cruise phase is over in case 1, and the EKF cannot obtain a satisfying result if the initial state has a large error. By contrast the UKF can adapt to these two different initial states and so does the WLS.

## 6 CONCLUSIONS AND DISCUSSION

Based on a future Mars program, this paper presents the processes of using optical autonomous navigation during the cruise phase to Mars. It includes the method of selecting asteroids used for navigation, obtaining the sequence of these asteroids, generating the observation data, and computing the OD by using WLS, EKF and UKF. Then two different initial state errors are set to evaluate the performance of the three filters.

Results indicate that both the WLS and the UKF have an excellent performance no matter if the initial state error is large or small. For WLS, 30 days can be chosen to be an optimal arc length over which data are acquired during the cruise phase to Mars, where the OD solution error is about 300~400 km in total position and 0.05~0.1 m s<sup>-1</sup> in total velocity. As a recursive processing algorithm, the UKF is able to converge quickly and reach a stable solution which is almost the same as

the WLS result in these two cases. However, the EKF can only get a good result in case 2, in which the initial error is small. Otherwise, it needs a long time to update the initial state. Therefore, the WLS and the UKF can be the first choice for optical autonomous navigation during the cruise phase to Mars.

The primary emphasis of this paper is to evaluate the capability of the three filters, namely that this paper aims to discuss the autonomous navigation OD algorithm. However, if either the WLS or UKF is applied in the optical autonomous navigation during a real mission to Mars, discussing the feasibility of actually implementing the autonomous OD process on a space mission is another important part of executing the task of autonomous navigation. In a real mission that uses autonomous navigation, designing a proper OD algorithm that incorporates autonomous navigation is just one key part of the whole mission. It also requires considerable computation, memory and data storage resources in the probe's platform. This represents a very complex problem in engineering.

**Acknowledgements** This work was supported by the National Natural Science Foundation of China (Grant No. 61179010).

## References

- Bhaskaran, S., Desai, S. D., Dumont, P. J., et al. 1998a, in AIAA/AAS Space Flight Mechanics Meeting
- Bhaskaran, S., Riedel, J. E., & Synnott, S. P. 1998b, in IEEE Aerospace Conference Proceedings, vol. 2, 353
- Bhaskaran, S., Riedel, J. E., Synnott, S. P., & Wang, T. C. 2000, in AIAA/AAS Astrodynamics Specialist Conference, AIAA-2000-3935
- Cao, J., Huang, Y., Hu, X., Ma, M., & Zheng, W. 2010, Chinese Science Bulletin, 55, 3654
- Chausson, L., & Delavault, S. 2003, in Proceedings of the 17th International Symposium on Space Flight Dynamics (<http://issfd.kiaml.rssi.ru/sessions.html>)
- Christian, J., & Lightsey, G. 2010, in AIAA SPACE 2010 Conference and Exposition, AIAA-2010-8786
- Daum, F. 2005, IEEE Aerospace and Electronic Systems Magazine, 20, 57
- Delavault, S., Berthier, J., & Foliard, J. 2004, in 18th International Symposium on Space Flight Dynamics, ESA Special Publication, 548, 467
- Jacobson, R. A. 1998, A&AS, 128, 7
- Julier, S. J., & Uhlmann, J. K. 1997, in Signal Processing, Sensor Fusion, and Target Recognition VI, Society of Photo-Optical Instrumentation Engineers (SPIE) Conference Series, 3068, ed. I. Kadar, 182
- Julier, S. J., & Uhlmann, J. K. 2004, Proceedings of the IEEE, 92, 401
- Long, A. C., Cappellari, J. O., Velez, C. E., & Fuchs, A. J. 1989, Goddard Trajectory Determination System (GTDS) Mathematical Theory (1st edn., Maryland: Goddard Space Flight Center, Computer Science Corporation, Lanham-Seabrook)
- MacKenzie, R., Lazaro Salvador, D., & Milligan, D. 2004, in 18th International Symposium on Space Flight Dynamics, ESA Special Publication, 548, 181
- Mastrodemos, N., Kubitschek, D. G., & Synnott, S. P. 2005, Space Sci. Rev., 117, 95
- Paluszek, M., Mueller, J., & Littman, M. 2010, in AIAA Infotech at Aerospace, AIAA-2010-3462
- Pittelkau, M. E. 2003, Journal of Guidance Control Dynamics, 26, 855
- Romanishin, W., & Tegler, S. C. 2005, Icarus, 179, 523
- Stastny, N. B., & Geller, D. K. 2008, Journal of Spacecraft and Rockets, 45, 290
- Tuckness, D. G., & Young, S.-Y. 1995, Journal of Spacecraft and Rockets, 32, 279
- VanDyke, M. C., Schwartz, J. L., & Hall, C. D. 2004, in Proceedings of the AAS/AIAA Space Flight Mechanics Conference
- Zanetti, R. 2009, Journal of Spacecraft and Rockets, 46, 865